Highly rarefied gas flows in rough channels of finite length

Zheng Shi,[1] Yulong Zhao,[2] Wei Su,[3, 4, *] and Lei Wu[1, †]

[1]*Department of Mechanics and Aerospace Engineering,*
Southern University of Science and Technology, Shenzhen 518055, China
[2]*State Key Laboratory of Oil and Gas Reservoir Geology and Exploitation,*
Southwest Petroleum University, Chengdu, Sichuan 610500, China
[3]*Division of Emerging Interdisciplinary Areas, The Hong Kong University*
of Science and Technology, Clear Water Bay, Hong Kong, China
[4]*Department of Mathematics, The Hong Kong University of Science and Technology, Clear Water Bay, Hong Kong, China*
(Dated: January 11, 2023)

The highly rarefied gas flow through a rough channel of finite length with small bumps appended to its surfaces is investigated, by varying the tangential momentum accommodation coefficient α in Maxwell's diffuse-specular boundary condition, the characteristic size and position of the bumps, and the channel length. First, we investigate the influence of the surface bumps and consider the rarefied gas flow in a unit channel with periodic boundary conditions to remove the end effect. It is found that the surface bumps have a significant impact on the flow capacity. The higher the bump, the more significant the obstructing effect on the gas flow. When α is very small (i.e., nearly specular reflection of gas molecules at the channel surface), the apparent gas permeability is dramatically reduced, even in the presence of small bumps, to a value that is almost comparable to the one when fully diffuse gas-surface scattering is assumed. This impact can be taken into account through an effective tangential momentum accommodation coefficient, i.e., the flow capacity of the rough channel is taken equivalently as that of a smooth channel without bumps but having gas-surface scattering under the effective tangential momentum accommodation coefficient. Second, we study the end effect by connecting a smooth channel of length L_0 to two huge gas reservoirs. It is found that (i) the end correction length is large at small α. Consequently, the mass flow rate barely reduces with increasing L_0 rather than scales down by a factor of $1/L_0$ as predicted by the classical Knudsen diffusion theory; and (ii) the end correction is related to the channel's aspect ratio. Finally, based on the effective tangential momentum accommodation coefficient and end correction, we explain the exotic flow enhancement in graphene angstrom-scale channels observed by Andre Geim's research group [Nature 558 (2018) 420].

I. INTRODUCTION

Permeability is the measure of flow capacity in porous media. It is a key parameter in a number of engineering applications, such as the commercial extraction of shale gas [1] and membrane separation [2]. In shale gas extraction, a considerably large value of permeability indicates exploitable shale gas, while how a system determines the actual fluid permeation and selectivity is an essential element in realizing practical membrane separation. Conventionally, the permeation of the low-speed flow through a porous medium is described by the Darcy law:

$$\overline{U} = -\frac{k}{\mu L_0}\Delta p, \qquad (1)$$

which demonstrates that the discharge per time $\overline{U}$ (in the unit of meter per second) is proportional to the permeability k (in the unit of square meter) and the pressure drop Δp over the porous medium, and inversely proportional to the medium length L_0 and the dynamic viscosity μ of the fluid. The permeability k, usually called intrinsic

permeability, is determined by the material and topological structure of the porous medium, and is irrespective of the fluid.

The Darcy law can be derived from the Navier-Stokes equations, for which the primary assumptions are sufficient intermolecular collisions among fluid molecules and non-slip velocity at the solid surface. However, these assumptions can be violated in gas transport with low density and small characteristic flow length, making the gas permeability no longer a constant for a given porous medium. For instance, in shale gas reservoirs, most of the gas is stored and transported in nanoscale matrix pores of 2-50 nm diameters [3–6], where the pore size is in the same order of magnitude as the mean free path of gas molecules so that gas-surface interactions begin to dominate over intermolecular collisions and apparent velocity slip appears at the solid boundary [7–10]. From a systematic experiment, Klinkenberg found that the slippage of gases along the pore surfaces gives rise to an enhanced permeability that increases with the reciprocal average gas pressure [11]. To distinguish it from intrinsic permeability, we call this permeability the apparent gas permeability (AGP) k_a. The enhancement of gas transport is also observed in atomically thin (angstrom-scale) structures such as carbon nanotubes and nano-porous films made from graphene and other two-dimensional (2D) materials [12, 13]. In such structures, the size of a transport

* weisu@ust.hk
† wul@sustech.edu.cn

channel is much smaller than the molecular mean free path; therefore, gas molecules are most likely to collide with the channel surface rather than each other. The emergence of angstrom-scale systems has offered new opportunities to develop separation membranes with ideal performance, high mechanical strength and chemical resistance [14].

The enhanced AGP is a consequence of the gas rarefaction effect, which can be understood through the Knudsen number Kn, defined as the ratio of the mean free path of gas molecules λ to the characteristic flow length H (i.e., the transverse dimension of the flow channel):

$$Kn = \frac{\lambda}{H} = \frac{\mu(T_0)}{\overline{p}H}\sqrt{\frac{\pi RT_0}{2}}, \qquad (2)$$

where $\overline{p}$ is the average gas pressure, T_0 is the gas temperature and R is the gas constant. Based on the value of Kn, gas transport mechanisms are roughly classified into continuum flow ($Kn < 0.001$), slip flow ($0.001 \leq Kn < 0.1$), transition flow ($0.1 \leq Kn < 10$) and free-molecular flow ($Kn \geq 10$). The Darcy law with intrinsic permeability is valid only for continuum flow. The Navier-Stokes equation equipped with proper slip-velocity boundary conditions are applicable for slip flow. Nevertheless, the continuum assumption breaks down in transition and free-molecular flows, so that the Navier-Stokes equations should be replaced by physical laws of gas kinetic theory, such as the Knudsen diffusion theory [15] and the Boltzmann equation [16].

In addition to the Knudsen number, experimental and numerical evidences have demonstrated the vital role of the gas-surface interaction in determining the gas transport properties of flows falling into the free-molecular regime [12, 15, 17]. In a recent experiment conducted by Andre Geim's research group, molecular flow rates of helium were measured in angstrom-scale 2D channels made from cleaved crystals such as the graphite, hexagonal boron nitride (hBN) and molybdenum disulfide (MoS_2). It was found that the gas transport rate strongly depends on wall materials [13]: the flow rate through MoS_2 channels can be predicted by the classical Knudsen diffusion theory, which is monotonously reduced as the channel length L_0 increases (with a scaling of $1/L_0$). On the contrary, the flow rate is further enhanced in graphene and hBN channels, which remains constant when the channel length enlarges. These observations were attributed to different materials exhibiting surfaces of different atomic landscapes. The MoS_2 surface with strong corrugations is relatively rough, where helium molecules are more likely to undergo diffuse scattering thus the Knudsen theory works well; however, the surfaces of graphene and hBN are much flatter and smoother, from which gas molecules can be specularly reflected without losing momenta. Besides the length dependence/independence, the magnitude of flow enhancement is also a function of channel height in the three types of channels.

Although surface corrugation and roughness can be used to qualitatively distinguish the different flow enhancements in channels with different materials, it cannot properly describe why the measured flow rate is a function of the channel height. Also, it cannot explain why the flow rate is not a function of the channel length in graphene and hBN channels. In this paper, we aim to quantify the free-molecular flow through rough channels of finite length and offer a comprehensive explanation of the results from Andre Geim's experiment [13]. The analysis is based on the numerical solution of the linearized Bhatnager-Gross-Krook (BGK) Boltzmann kinetic model equation [18]. Surface corrugation is modeled by small bumps appended to the channel surface, and gas-surface scattering is described by the classical Maxwell's diffuse-specular boundary condition. Thus, the surface roughness is characterized by the bump size and position, as well as the tangential momentum accommodation coefficient (TMAC) in Maxwell's boundary condition. Since the molecular diffusion along the solid surface is negligible [19], we shall focus on the dependence of AGP on the surface corrugation, the TMAC, and the end effect caused by the finite channel length. We emphasis that although the molecular dynamics simulation can be used to investigate gas transport through nano- and sub-nano-channels [20, 21], it is not effective in evaluating the end effect involving large system sizes due to massive computational consumption.

The rest of this paper is constructed as follows. In Sec. II, the linearized BGK model equation and the numerical scheme are briefly described. In Sec. III, numerical simulations are performed to analyze how the AGP in a unit channel varies with the Knudsen number, the bump size and position, and the TMAC. In Sec. IV, the end effect is investigated by connecting a channel with finite length to two large gas reservoirs. In Sec. V, we provide a reasonable explanation for the observation in Andre Geim's experiment. Conclusions are given in Sec. VI.

II. GAS KINETIC THEORY

As shown in Fig. 1, we consider a 2D pressure-driven gas flow between two parallel plates in a Cartesian coordinate system. The ends of the channel are connected to two large reservoirs containing gas at different pressures. Rectangular bumps, each with height h and width w, are attached to the inner channel surfaces and distributed periodically along the horizontal direction. The adjacent upper and lower bumps are separated by a distance of 2δ. When $\delta = 0$, bumps are symmetrically distributed on the inner surfaces.

We assume that the pressure difference at the two gas reservoirs is small, so that the linearized kinetic equation can be used. This assumption implies that the transport rate of the gas flow would be linearly proportional to the pressure difference, which agrees well with the experimental observations [13]. The following linearized BGK-Boltzmann kinetic equation is adopted to describe
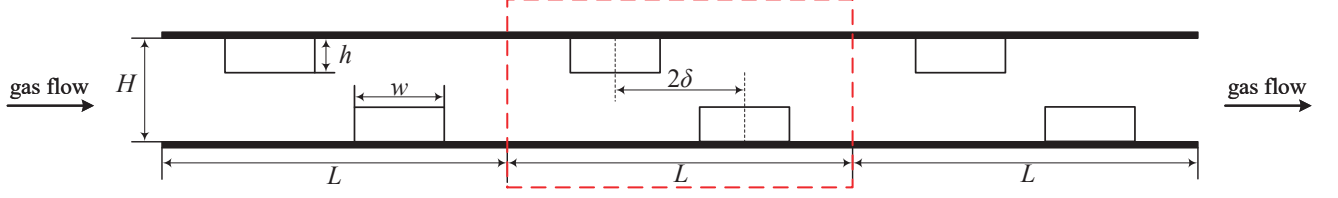
FIG. 1: Schematic of a gas flow through a two-dimensional channel with bumps attached on the inner surfaces. The height and width of the bumps is h and w, respectively, while the bump offset is 2δ. If the channel is sufficiently long, then the gas kinetic theory can be applied only in the unit cell (inside the red box) to save computational resources.

the rarefied gas dynamics [22]:

$$\frac{\partial h}{\partial t} + \boldsymbol{v} \cdot \frac{\partial h}{\partial \boldsymbol{x}} = \frac{\sqrt{\pi}}{2Kn}\left(n + 2\boldsymbol{U} \cdot \boldsymbol{v} - h\right), \qquad (3)$$

where $h(\boldsymbol{v}, \boldsymbol{x})$ is the velocity distribution function, $\boldsymbol{v} = (v_1, v_2)$ is the molecular velocity normalized by the most probable speed $v_m = \sqrt{2RT_0}$ of gas molecules, and $\boldsymbol{x} = (x_1, x_2)$ is the spatial coordinate normalized by H, with the subscripts "1" and "2" denoting the horizontal and vertical directions, respectively. The number density n and the macroscopic flow velocity $\boldsymbol{U} = (U_1, U_2)$ are calculated via the velocity distribution function as

$$n = \iint h f_{eq} dv_1 dv_2,$$

$$\boldsymbol{U} = \iint \boldsymbol{v} h f_{eq} dv_1 dv_2, \qquad (4)$$

where $f_{eq} = \exp(-v^2)/\pi$ is the equilibrium velocity distribution function, so that Eq. (3) is an integro-differential equation. The temperature of the solid surface is maintained at T_0.

Although the Boltzmann equation is well validated in describing rarefied gas dynamics, such as normal shock wave and sound wave propagation [23], so far the gas-surface interaction still relies on empirical model and parameters [24]. In this paper we consider the widely used Maxwell's diffuse-specular boundary condition, where the impinged molecules reflected from the solid wall undergo diffuse and specular reflections, and the ratio of the number of diffuse reflections is quantified by the TMAC α. Pure diffuse and specular reflections have $\alpha = 1$ and 0, respectively. And the smaller the value of α, the larger the flow rate in the transition flow and free-molecular flow regimes, due to the less loss of momentum. In this linearized problem, the Maxwell's diffuse-specular boundary condition at the solid surface reads [25]:

$$h(\boldsymbol{x}, \boldsymbol{v}) = (1 - \alpha)h(\boldsymbol{x}, \boldsymbol{v} - 2\boldsymbol{n}v_n)$$
$$+ \frac{2\alpha}{\sqrt{\pi}} \int_{v'_n < 0} |v'_n| h(\boldsymbol{x}, \boldsymbol{v}') \exp(-v'^2) dv'_1 dv'_2, \quad (5)$$

where $\boldsymbol{n}$ is the outer normal vector of the solid surface, and v_n is the velocity component in the normal direction.

The kinetic equation is solved by the deterministic discrete velocity method [26], where the molecular velocity space $\boldsymbol{v}$ is represented by a set of discrete velocities. To capture the discontinuities in the velocity distribution function at large Knudsen numbers [27, 28], v_1 and v_2 are discretized by $N_v = 72$ non-uniform points in each direction:

$$v_{1,2} = \frac{5}{(N_v - 1)^3}(-N_v + 1, -N_v + 3, \cdots, N_v - 1)^3. \quad (6)$$

The spatial region is also divided non-uniformly, with refined grid points near the solid wall. The discretized kinetic equation is solved by the general synthetic iterative scheme [29, 30], where the iteration is terminated when relative error in the dimensionless mass flow rate:

$$G_p = \int_0^1 U_1(x_2) dx_2 \qquad (7)$$

between two consecutive iteration steps is less than 10^{-5}.

III. RESULTS WITHOUT THE END EFFECT

We first consider the case where the channel is sufficiently long, so that the end effect at the inlet and outlet can be neglected [31, 32]. Under this circumstance, we do not need to simulate to whole channel and reservoirs, but only the unit cell, denoted by the red box, of the size $H \times L$, see Fig. 1. In addition to Maxwell's boundary condition at the solid walls, the following periodic boundary conditions are used on the left and right boundaries of the unit channel [16]:

$$\begin{cases} h(0, x_2, \boldsymbol{v}) = 1 + h\left(\frac{L}{H}, x_2, \boldsymbol{v}\right), & \text{when } v_1 > 0, \\ h\left(\frac{L}{H}, x_2, \boldsymbol{v}\right) = -1 + h(0, x_2, \boldsymbol{v}), & \text{when } v_1 < 0, \end{cases} \quad (8)$$

implying that the flow is driven by the unit pressure gradient pointed to the negative direction of x_1. The AGP, which is normalized by H^2, is calculated as

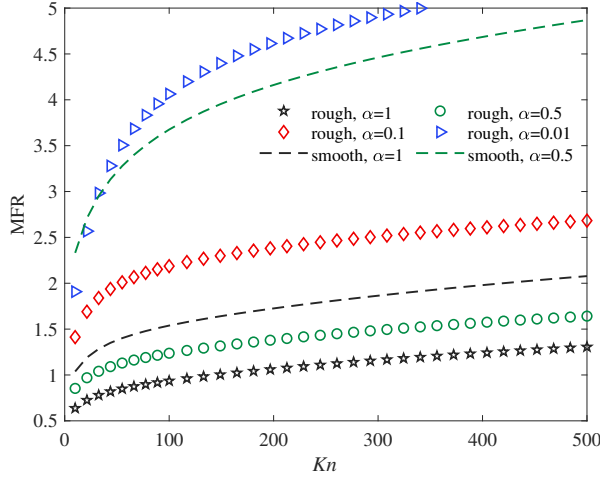$$k_a = \frac{2Kn}{\sqrt{\pi}} G_P. \qquad (9)$$

FIG. 2: The dimensionless mass flow rate as a function of the Knudsen number, with different values of TMAC. The size of the unit channel is $H \times H$. In the rough channel, each bump has a size of $h \times w = 0.1H \times 0.2H$, and the offset distance is $\delta = 0$.

We consider the rarefied gas flow in the free-molecular flow regime as relevant to the experiment [13]. In this case, for flow through two parallel, infinite, and smooth (i.e., without small bumps) plates, it is well known that the dimensional mass flow rate is a logarithmic function of the Knudsen number, while for flow through a smooth channel with two-dimensional cross-section, the mass flow rate will approach a constant [33]. Figure 2 shows that, even in the presence of bumps of size $h \times w = 0.1H \times 0.2H$, the flow rate increases logarithmically with the Knudsen number. Without loss of generality, we can consider the representative case of $Kn = 10$ in the following paper.

It is well known that, for a smooth channel without bumps, the mass flow rate is a function of the TMAC, which is roughly proportional to $(2-\alpha)/\alpha$. For instances, when $\alpha = 0.1$ and 0.01, the mass flow rate at $Kn = 10$ is 10.5 and 90.9, which are larger than 1.038 under fully diffuse gas-surface scattering by one and two orders of magnitude, respectively. Therefore, the flow rate of rarefied gas flow through channels with near-specular-reflection surfaces (i.e., TMAC close to zero) is much larger than that through channels with diffusive surfaces. However, when the bumps are added to the surfaces of a smooth channel, the mass flow rate under a small TMAC of $\alpha = 0.01$ is dramatically reduced, to a value that is almost comparable to that of the smooth channel with $\alpha = 0.5$; see Fig. 2. A similar behavior is also observed in the hypersonic flow in the slip flow regime [34]. In this section, we try to pinpoint the major factors that cause this huge reduction.
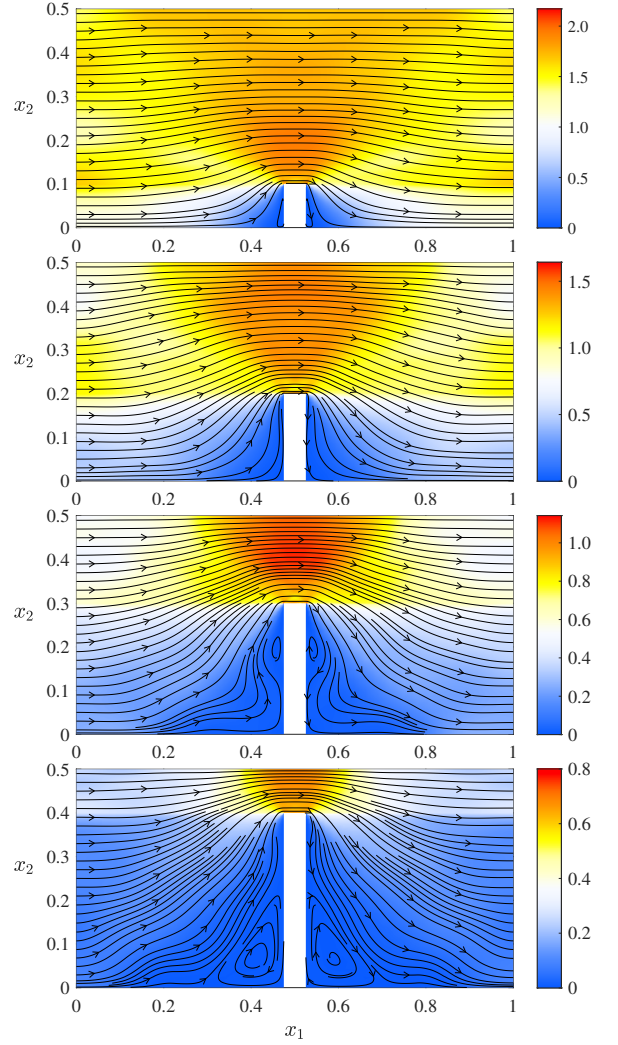

FIG. 3: Streamlines and magnitude of velocity in lower half of the unit channel having a size of $H \times H$, when TMAC=0.01 and $w = 0.05H$. From top to bottom, the height of the bump is $h = 0.1H$, $0.2H$, $0.3H$, and $0.4H$, respectively.

A. Bump Height

We fix the bump width, and the bump offset at $\delta = 0$, but vary the bump height to systematically investigate its influence on the flow velocity and the AGP. The unit cell (red box in Fig. 1) considered has a size of $H \times H$.

Figure 3 depicts the streamlines and the magnitude of flow velocity in the bottom half unit cell, when the TMAC is $\alpha = 0.01$. The bumps directly disturbs the velocity profile of the channel, where the corner hinders the gas flow's capability to approach the wall, resulting in significant energy loss and reduction of boundary velocity slip. With the increase of bump height, the amount of vortices near the corner increases. The region in which flow velocity is close to zero begins to extend to both ends of the unit channel. The mass flow rate is greatly

FIG. 5: The AGP as a function of the bump height. The unit channel size is $H \times H$. The bump width is fixed to be $0.2H$, and the offset distance $\delta = 0$. Note that in the inset, $\tilde{h} = 0.5H - h$.
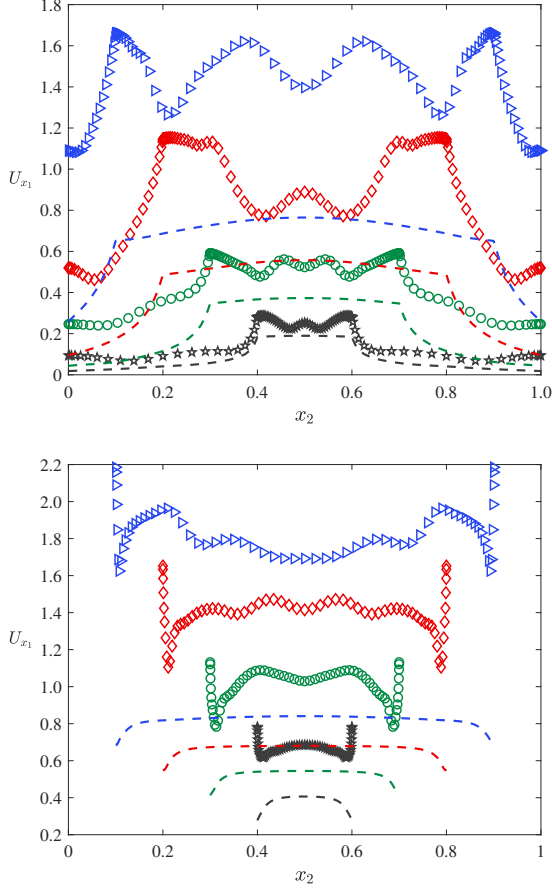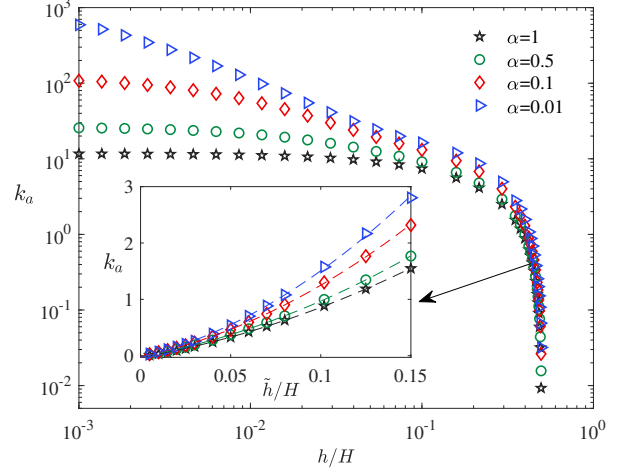
FIG. 4: Horizontal velocity profiles for different values of bump height, when the bump width is $w = 0.05H$. (Top) at inlet: $x_1 = 0$. (Bottom) at the middle of channel: $x_1 = 0.5H$. Symbols: TMAC=0.01. Lines: TMAC=1. In each figure, in each group of line styles, from top to bottom, the bump height is $h = 0.1H$, $0.2H$, $0.3H$, and $0.4H$, respectively.

reduced, not only because the effective channel height is smaller, but also because the peak flow speed drops. The streamlines and velocity magnitude for other values of TMAC are more or less the same.

Figure 4 shows the velocity distribution in the x_1 direction at the inlet and middle of the channel, when $\alpha = 1$ and $\alpha = 0.01$. When the fully diffuse boundary condition is considered, we see that the flow's horizontal velocity gradually increases from the solid surface to the channel center, and the maximum horizontal speed appears in the channel center ($x_2 = 0.5H$). However, when the near-specular boundary condition (e.g. $\alpha = 0.01$) is considered, the horizontal speed at the channel inlet does not monotonically increase from the channel surface to center, but has several peaks. Moreover, at $x_1 = 0.5H$, the maximum horizontal speed does not appear at the channel center ($x_2 = 0.5H$), but at the top surface of the bump. In other words, the velocity profile is in-

verted, which is contrast to the conventional pressure-driven flow.

When the bump height increases, it is seen from Fig. 4 that the velocity slip near the wall decreases. Near the solid surface, the higher the bump height, the more frequent the collision between the gas molecules and the wall, the more serious the energy loss, resulting in the decrease of the velocity near the wall. At the same height as the bump ($x_2 = h$), the velocity reaches the peak.

Figure 5 shows the effect of bump height on the AGP at different TMAC. It is seen that, when the TMAC is fixed, when the bump height is very small, the change of bump height has almost no effect on the AGP. As the bump height gradually increases, the smaller the value of TMAC, the more sensitive of the AGP to the change of bump height. When the bump height increases to a certain extent, the AGP decreases dramatically with the increase of bump height. In fact, when the bump height approaches 0.5, the permeability is dominated by this small channel (formed by bumps) of effective height $H - 2h$. Since in the straight channel the permeability is proportional to the height square, we see in the inset of Fig. 5 that the AGP is approximately a quadratic function of $\tilde{h} = 0.5H - h$.

B. Bump Width

To investigate the effects of bump width on the AGP, the height of the bumps is fixed at $h = 0.1H$ and $0.01H$, respectively, and the TMAC is chosen to be 0.01. The numerical results are visualized in the left plot in Figure 6. When the bump width is $w = 0$, there are literally no bumps, the inner surface of channel is completely smooth, and the AGP is large due to the large propor-
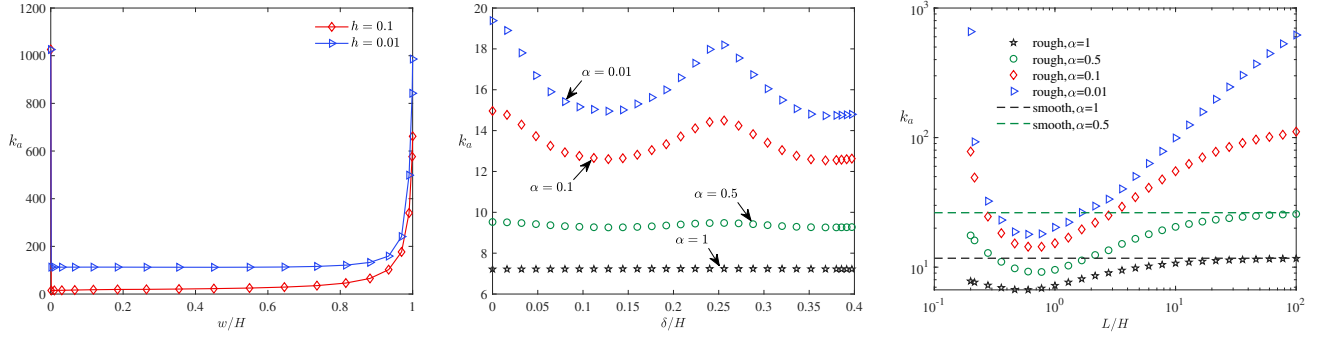
FIG. 6: (Left)The AGP as a function of the bump width. The offset distance is $\delta = 0$. (Middle) The AGP as a function of the offset distance δ. The bump size is $0.1H \times 0.2H$. In both figures, the unit channel size is $H \times H$ and the TMAC is 0.01. (Right) The AGP as a function of channel length. The bump size is $0.1H \times 0.2H$, and the offset distance is $\delta = 0$.

tion of specular reflection at the solid surface. When the bump width increases only a little bit, so that the bumps look like thin plates, the AGP drops dramatically: the higher the bump, the larger the drop. Then, the AGP remains nearly unchanged when the bump width gradually increases to up $w = 0.8H$. When the bump width gradually approaches the whole channel length $w = H$, we see a rapid surge in the AGP. This is because now the distance between the bumps is very narrow and the channel can be viewed as the smooth channel again. In the limit of $w = H$, the AGP is slightly smaller than that of $w = 0$, because the effective channel height is now reduced from H to $H - 2h$. This example shows that the bump height plays a significant role in the AGP reduction, rather than the bump width.

C. Bump Offset Distance

Since the distribution of rough elements is random in the realistic scene (when the channel adsorbs some impurities, such as the PMMA polymer molecules on the graphene surface [13]), a single simplified model may not be accurate enough in describing the gas flow through a real rough channel. However, it can be seen from the middle plot in Fig. 6 that, the changes in bump distribution, through adjusting the offset distance δ, does not significantly affect the AGP. For example, the variation of AGP with respect to δ increases when the TMAC decreases, but even when $\alpha = 0.01$ the highest to the lowest AGP is only about 1.3 over the whole range of bump offset.

D. Unite Channel Length

Now we fix the channel height, and the bump size and position, but increase the unit channel length L to see its effect on the AGP. The value of L represents the spacing among the repeated bumps in the full channel. As is

shown in the right plot in Fig. 6, when the channel length is infinitely close to the bump width, the channel is equivalent to a smooth channel, which causes a high AGP. As the unit channel length increases, the surface of channel becomes rough and the obstruction to gas flow increases, so the AGP decreases gradually. Note that there is still a sudden drop in the initial process of increasing the channel length from $L = 0.2H$, the reason of which is explained in Sec. III B. The location of the minimum AGP is about $L/H = 0.6$. When the channel length increases to a certain degree, the flow space of the channel become larger and larger, which leads to an increase in AGP. Finally, with the continuous increase of the channel length, the AGP tends to saturate. The position where the AGP tend to saturate increases with the decrease of TMAC. For example, when the TMAC is 1 and 0.1, the location occurs at $L/H = 60$ and $L/H = 100$, respectively.

E. Effective TMAC

The reduction of AGP at a small value of TMAC in the rough channel with surface bumps can be taken into account through an effective TMAC, where the flow capacity of the rough channel is equivalent to that through a smooth channel without bumps but having gas-surface scattering under the effective TMAC. Since the AGP is not sensitive to the bump width and bump offset distance, here we investigate the effective TMAC of the rough channel by fixing the bump width at $w = 0.2H$ and offset distance at $\delta = 0$. We still consider the unit channel of size $H \times H$, see the red box in Fig. 1. The effective TMAC is determined in the following manner. First, we choose the TMAC=1, and calculate the AGP of rough channel at $Kn = 10$. Then, we choose a smooth channel with TMAC=1, and adjust the channel height to make its AGP equal to that of the rough channel. Finally, we get the AGP of the rough and smooth channels at different values of TMAC; by equating the AGP of the rough channel to that of the smooth channel, we de-
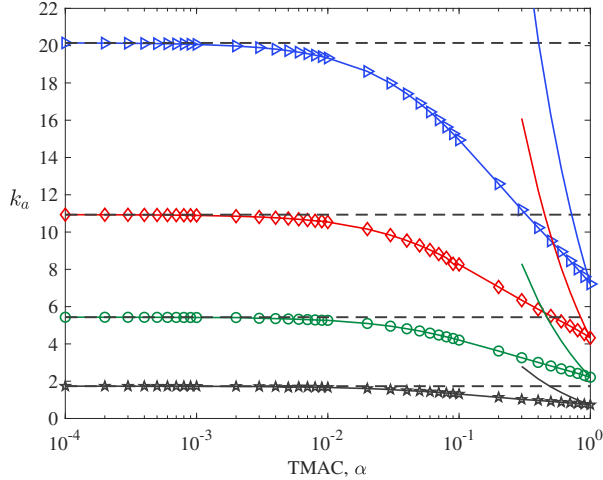
FIG. 7: The effective TMAC, when the unit channel size is $H \times H$. In each group of line styles, from top to bottom, the bump height is $h = 0.1H$, $0.2H$, $0.3H$, and $0.4H$, respectively. The solid lines, from top to bottom, show the AGP of the smooth channel with heights of $0.766H$, $0.578H$, $0.400H$, and $0.218H$, respectively. The bump width is fixed at $w = 0.2H$.
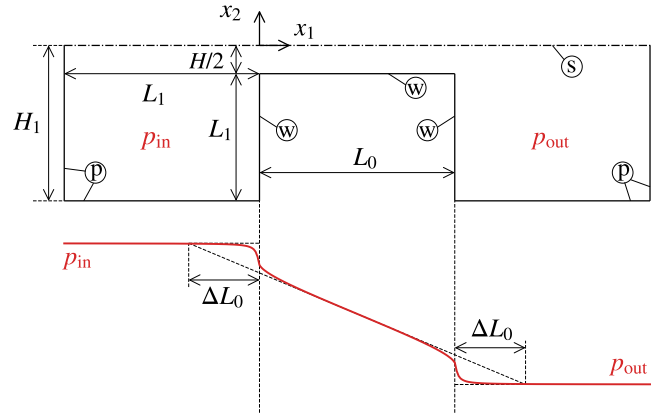

FIG. 8: Schematic of the computational domain and pressure distribution to quantify the end effect at small TMACs. A 2D channel with a size of $L_0 \times H$ is connected to two large reservoirs filled with gas maintained at pressures p_{in} and p_{out}, respectively. The flow field is simulated on the lower half of the geometry due to symmetry. No bumps are appended to the channel surfaces. The distribution of gas pressure along the horizontal center line (dash-dotted line) for TMAC $\alpha = 0.1$ is shown in solid red line. End effect causes pressure jump at the inlet/outlet of the channel and can be taken into account by the increment ΔL_0 to the channel length [32].

termine the effective TMAC of the rough channel to be that of the smooth channel (see the points of intersection between the dashed lines and solid lines in Fig. 7). For example, in Fig. 7 we see that, when $\alpha = 1$, the AGP of the rough channel with bump size $h \times w = 0.1H \times 0.2H$ is the same as that of the smooth channel with a height of $0.766H$. When the TMAC of this rough channel is less than 0.001, the effective TMAC of this channel is about 0.404. Similarly, when the rough channel has bump heights of $0.2H$, $0.3H$, and $0.4H$, the effective channel height of the smooth channel is $0.578H$, $0.400H$, and $0.218H$, while the effective TMAC of the rough channel (when the true TMAC is very small) is 0.451, 0.468, and 0.491, respectively. Thus, a small bump results in a huge reduction of permeability, or equivalently, a big increase of the effective TMAC.

In the limit of $h \to 0$, and the true TMAC approaches zero, the effective TMAC, as obtained in the numerical simulation, can be approximately given by

$$\alpha_{\text{effective}} \approx 10 \frac{h}{H}, \tag{10}$$

while the enhancement ratio K, i.e., the permeability normalized by the permeability obtained from the diffuse scattering, is

$$K \approx \frac{1}{\alpha_{\text{effective}}} \approx 0.1 \frac{H}{h}. \tag{11}$$

IV. END EFFECT

In the previous section, we considered gas flows between two parallel and infinitely long plates, where the end effect (i.e., pressure loss at the inlet and outlet of a finite channel) is neglected. Nevertheless, in an experiment, flow rates are usually measured through channels of finite lengths, where the ends of a channel are connected to two large reservoirs maintained at different conditions (e.g., containing gases with different pressures to drive the flow by pressure gradient). The influence of the inlet and outlet ends also contribute to the length dependence of the flow rate. Based on the concept of effective channel length, end corrections for flow rates of rarefied gases through moderate long tubes were developed under the assumption of fully diffuse gas-surface scattering [31, 32]. In this section, we investigate the end effect when pure diffuse scattering breaks down.

The schematic diagram of the computational domain is illustrated in Fig. 8. A 2D channel having a size of $L_0 \times H$ is connected to two large reservoirs that are filled with gas maintained at pressures of p_{in} and p_{out} with $p_{\text{in}} > p_{\text{out}}$, respectively. Consequently, the gas is driven from the left reservoir to the right one. The origin of horizontal axis x_1 is fixed at the center of the inlet cross section of the channel. An expected pressure distribution along the horizontal center line (dash-dotted line) is also

plotted. It shows that the gas pressure varies linearly inside the channel at locations far from its inlet and outlet ends; but the linear dependence changes in the areas around the inlet and outlet of the channel and the pressure eventually approaches the values in reservoirs. The end effect causes a pressure jump at the inlet (outlet) cross section, i.e., $x_1 = 0$ ($x_1 = L_0/H$), where the pressure is not equal to p_{in} (p_{out}). As a consequence, the true flow rate is smaller than that of the flow driven by the constant pressure gradient $(p_{\text{in}} - p_{\text{out}})/L_0$ in a sufficiently long channel. This effect can be quantified by the length increment ΔL_0 to the total channel length [32]. Then, the Darcy law (1) should be modified to

$$G_p = -\frac{\sqrt{\pi}}{2Kn}\frac{k_a}{(L_0 + 2\Delta L_0)/H}\Delta p, \qquad (12)$$

where k_a is the AGP of the infinite long channel and $\Delta p = (p_{\text{out}} - p_{\text{in}})/\bar{p}$ is the gas pressure difference between the outlet and inlet reservoirs normalized by the average gas pressure. Note that the relation (12) is presented in a dimensionless form with $G_p = \overline{U}/v_m$, i.e., the dimensionless mass flow rate (7). is equal to the discharge per time normalized by the most probable speed v_m of gas molecules. Again, we consider the representative case of $Kn = 10$.

A. Numerical Settings

To determine the pressure jump and incremental length for flows in angstrom-scale channels under gas-surface interactions with different values of TMAC, we choose four TMACs $\alpha = 1, 10^{-1}, 10^{-2}, 10^{-4}$. A small pressure difference is imposed, i.e., $(p_{\text{in}} - p_{\text{out}}) \ll p_{\text{in}}$; thus, the pressure jumps (or the length increments) at the inlet and outlet cross sections are identical. To demonstrate the length dependence of the flow rate, we consider the channel length in the range of $L_0/H \in [5, 5000]$. The dimension of simulation domain for each reservoir is $L_1 \times H_1$ with $H_1 = H/2 + L_1$. As shown in Fig. 8, the boundaries labeled by '(w)' are solid surfaces, with the boundary condition given in Eq (5); these labeled by '(p)' are pressure inlet/outlet boundaries, where the boundary condition is specified as

$$\begin{cases} h(\boldsymbol{x}, \boldsymbol{v}) = (p_{\text{in}} - \bar{p})/\bar{p}, & \text{for } \boldsymbol{v}\cdot\boldsymbol{n} \geq 0 \text{ at inlet,} \\ h(\boldsymbol{x}, \boldsymbol{v}) = (p_{\text{out}} - \bar{p})/\bar{p}, & \text{for } \boldsymbol{v}\cdot\boldsymbol{n} < 0 \text{ at outlet;} \end{cases}$$
$$(13)$$

and the horizontal center line labeled by '(s)' is a symmetry boundary: $h(\boldsymbol{x}, v_1, v_2) = h(\boldsymbol{x}, v_1, -v_2)$. The macroscopic flow properties of interest are gas pressure and flow velocity. In an isothermal case, the gas pressure is related to the number density n [calculated according to Eq. (4)] through

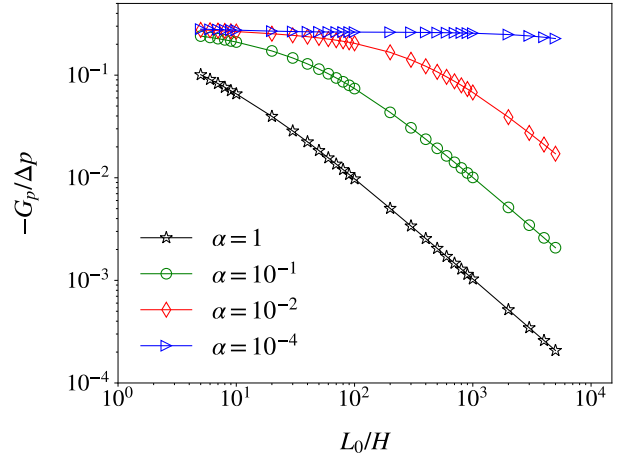$$\frac{p}{\bar{p}} - 1 = n. \qquad (14)$$

FIG. 9: Dimensionless mass flow rate in a channel with finite length.

The discontinuous Galerkin method is employed to discretize the kinetic equation (3) in the spatial space, where the computational domain is partitioned by regular disjoint triangles. In order to obtain grid-independent results, we run the simulation on meshes with different triangle sizes to ensure that a further mesh refinement does not change the pressure and velocity fields with magnitudes larger than 0.5%. We also repeat the simulation to determine the size of L_1 and make sure that the results are independent of the reservoir size. Eventually, $L_1/H = 50$ is chosen for all considered cases. Non-uniform meshes with refinement near the solid surfaces are used, where the cell sizes (the height of a triangle, h_Δ) vary in $0.1 \leq h_\Delta/H \leq 7$. The other computational parameters are the same as those used in the previous sections. Note that the flow is essentially multiscale, so the general synthetic iterative scheme [29] is used here to boost the convergence in numerical simulations.

B. Mass Flow Rate

The dimensionless mass flow rate G_p divided by $-\Delta p$ as functions of the channel length is illustrated in Fig. 9 for different values of TMAC. It is found that the mass flow rate has relatively small values when the fully diffuse gas-surface interaction is enforced. Besides, it scales down approximately by a factor of $1/L_0$ when the channel length increases. Driven by the same pressure difference, the mass flow rate is largely enhanced when the TMAC is decreased. When the TMAC is reduced to $\alpha = 10^{-4}$, i.e., most of the gas molecules are specularly reflected from solid surfaces, the mass flow rate remains constant when the channel length varies within the considered range. Consequently, the mass flow rate of $\alpha = 10^{-4}$ can be three orders of magnitude larger than that of $\alpha = 1$ in a relatively long channel (e.g., $L_0/H = 5000$). The mass flow rates with $\alpha = 0.1$ and 0.01 also decrease with in-
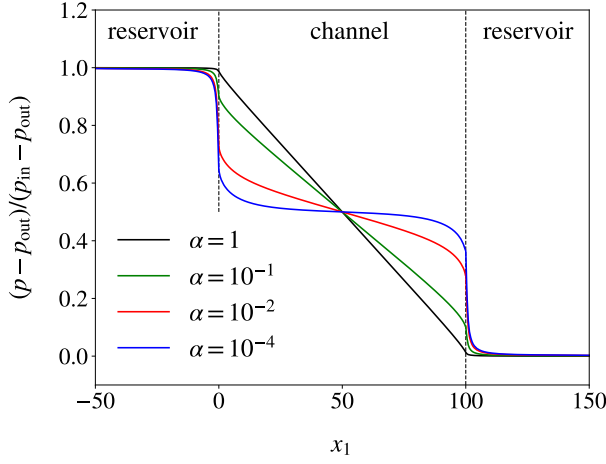
FIG. 10: Normalized pressure distribution along the horizontal center line of a channel connecting to two gas reservoirs. The channel length is $L_0/H = 100$.

creasing channel length, but it is much slower than the scaling of $1/L_0$ under $\alpha = 1$.

C. End Correction Length

In order to understand how the inlet and outlet ends of the channel affect the gas flow, we plot the gas pressure distribution along the horizontal center line of the channel connecting to two gas reservoirs in Fig. 10. The channel length is $L_0/H = 100$. It is shown that the pressure changes nearly with a constant gradient m_α in the central area of the channel that is remote from the inlet and outlet of the channel. That is, the pressure inside the channel, say $0.3L_0/H \leq x_1 \leq 0.7L_0/H$, can be fitted as

$$\frac{p - p_{\text{out}}}{p_{\text{in}} - p_{\text{out}}} = m_\alpha \left(x_1 - \frac{L_0}{2H} \right) + \frac{1}{2}. \quad (15)$$

The absolute value of the gradient m_α decreases with the TMAC; consequently, for a given length L_0, the channel with a smaller TMAC suffers larger end effect, where the gas pressure varies significantly in the vicinity of the inlet and outlet. These trends hold for channels with other lengths.

To quantify the end effect, we calculate the length increment ΔL_0; the larger the length increment, the significant the end effect will be. As shown in Fig. 8, it is defined as the distance between the inlet (outlet) cross section and the position at which the pressure reaches p_{in} (p_{out}) according to the linear extrapolation of the pressure curve inside the channel; from some algebraic calculations, we have

$$\frac{\Delta L_0}{H} = -\frac{1}{2m_\alpha} - \frac{L_0}{2H}. \quad (16)$$

The increment ΔL_0 for selected channel length and different TMACs are listed in Table I. It is shown that for

TABLE I: End effect for channel with finite length: the length increment ΔL_0 obtained from Eqs. (15) and (16).

L_0/H	α	$\Delta L_0/H$	$1/[(L_0 + 2\Delta L_0)/H]$
5	1	1.258×10^0	1.331×10^{-1}
	10^{-1}	7.020×10^0	5.252×10^{-2}
	10^{-2}	1.359×10^1	3.107×10^{-2}
	10^{-4}	1.533×10^1	2.805×10^{-2}
10	1	1.595×10^0	7.581×10^{-2}
	10^{-1}	9.731×10^0	3.394×10^{-2}
	10^{-2}	2.268×10^1	1.806×10^{-2}
	10^{-4}	2.695×10^1	1.565×10^{-2}
20	1	2.051×10^0	4.149×10^{-2}
	10^{-1}	1.325×10^1	2.151×10^{-2}
	10^{-2}	4.219×10^1	9.580×10^{-3}
	10^{-4}	5.798×10^1	7.355×10^{-3}
50	1	2.698×10^0	1.805×10^{-2}
	10^{-1}	1.788×10^1	1.166×10^{-2}
	10^{-2}	9.926×10^1	4.024×10^{-3}
	10^{-4}	2.484×10^2	1.829×10^{-3}
100	1	2.911×10^0	9.450×10^{-3}
	10^{-1}	1.997×10^1	7.146×10^{-3}
	10^{-2}	1.497×10^2	2.504×10^{-3}
	10^{-4}	1.191×10^3	4.028×10^{-4}
200	1	3.136×10^0	4.848×10^{-3}
	10^{-1}	2.056×10^1	4.147×10^{-3}
	10^{-2}	1.700×10^2	1.852×10^{-3}
	10^{-4}	7.401×10^3	6.666×10^{-5}
500	1	4.801×10^0	1.962×10^{-3}
	10^{-1}	1.910×10^1	1.858×10^{-3}
	10^{-2}	1.729×10^2	1.182×10^{-3}
	10^{-4}	1.674×10^4	2.944×10^{-5}
1000	1	5.530×10^0	9.891×10^{-4}
	10^{-1}	9.757×10^0	9.809×10^{-4}
	10^{-2}	1.724×10^2	7.436×10^{-4}
	10^{-4}	1.647×10^4	2.947×10^{-5}
2000	1	5.656×10^0	4.972×10^{-4}
	10^{-1}	6.036×10^0	4.970×10^{-4}
	10^{-2}	1.604×10^2	4.309×10^{-4}
	10^{-4}	1.524×10^4	3.079×10^{-5}
5000	1	5.676×10^0	1.995×10^{-4}
	10^{-1}	6.932×10^0	1.994×10^{-4}
	10^{-2}	3.054×10^1	1.976×10^{-4}
	10^{-4}	1.471×10^4	2.905×10^{-5}

a fixed channel length, ΔL_0 increases with decreasing TMAC.

Figure 9 shows that the mass flow rate scales down with the channel length by a factor of $1/L_0$ under fully diffuse gas-surface scattering, but remains constant when the TMAC is rather small. This can be explained by the end correction length. The dimensionless mass flow rate can be estimate by the Darcy law (12) when the channel length is relatively long, say, $L_0/H \geq 500$. Note that for a channel without small bumps, the gas permeability k_a is independent on L_0, although its values are different for
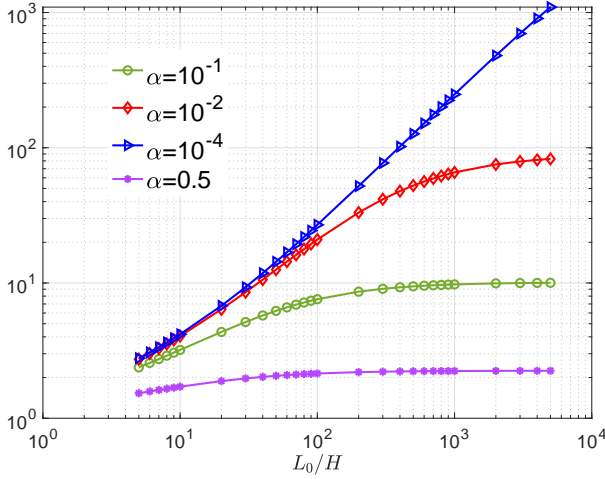
FIG. 11: Enhancement (i.e. the mass flow rate normalized by that of the finite-length channel with the diffuse scattering) of the mass flow rate as a function of the channel length.

different TMACs. Therefore, for a given α, we have

$$-\frac{G_p}{\Delta p} \propto \frac{1}{(L_0 + 2\Delta L_0)/H}. \tag{17}$$

The quantities $1/[(L_0+2\Delta L_0)/H]$ are listed in the fourth column of Table I, which can be approximated as

$$\frac{1}{(L_0 + 2\Delta L_0)/H} \simeq \begin{cases} 0.98\frac{1}{L_0/H}, & \text{for } \alpha = 1, \\ 2.9 \times 10^{-5}, & \text{for } \alpha = 10^{-4}, \end{cases} \tag{18}$$

when $500 \leq L_0/H \leq 5000$. Therefore, when the TMAC is sufficiently small, the end effect is so intensive that the mass flow rate is independent on the channel length.

D. Flow Enhancement

With the data in previous sections, we visualize the flow enhancement coefficient K (i.e. the ratio of the measured flow rate to the value calculated by the Knudsen theory) in Fig. 11. It is found that, when the TMAC is fixed, as the channel length increases, the enhancement coefficient first increases with the channel length linearly, and then saturates to a value which is roughly given by Eq. (11). When effective TMAC is small, the linear increase of enhancement with the channel length is also observed in Ref. [19], see Fig. 3(b) therein. Also, when the channel length is fixed, but the channel height increases, the enhancement coefficient decreases because L_0/H decreases, this is consistent with the molecular dynamic simulation in Ref. [19], see Fig. 3(b) there. This comparisons demonstrates the reliability of our kinetic treatment of the gas flow problem.

V. EXPLANATION OF EXPERIMENT

Based on the numerical findings in the previous two sections, we are now in the position to explain the experimental phenomenon observed by Andre Geim's research group [13]. First, it is found that the permeability in graphite and hBN devices is not a function of the channel length L_0, while the permeability in MoS_2 channel scales down as $1/L_0$, see Fig. 2(b) in Ref. [13]. Since in the experiment the ratio between channel length and height is about 10^3 (i.e., the channel height is about 1.36 nm, while the length varies from 1 to 15 μm), from Fig. 9 it can be inferred that the graphite and hBN devices have an effective TMAC of $10^{-3} \sim 10^{-4}$ (i.e., gas molecules undergo near-specular scattering at the channel surface), while the MoS_2 channel has effective TMAC $\alpha \sim 1$ (i.e., gas molecules undergo diffuse scattering at the channel surface). Were the graphite and hBN devices made longer, the mass flow rate would begin to decrease.

Second, it is found in the experiment that "within the data scatter, the gas flow through MoS_2 channels is described well by the Knudsen theory of diffuse scattering, while all graphite and hBN devices exhibited strong enhancement reaching $K > 100$". For the latter devices, when the channel height is small, K increases with the channel height [13]. This can be understood as follows. When the height increases, the ratio between the channel height and the bump height increases, so that according to Eq. (10) the effective TMAC decreases, and the enhancement ratio increases. In the experiment K is about 100, then according to the data in Fig. 11 the effective TMAC is about 10^{-2}. Therefore, as per Eq. (10), the bump height to the channel height is about 10^{-3}, which indicates an atomically-flat surface. We notice that, at each channel height, the experimentally measured enhancement has large error bars, for instance, when $H = 1.36$ nm, K varies from 80 to 300 [13]. This may be attributed to the fact that in the experiment the channel length varies significantly, so that according to Fig. 11 the enhancement also has a significant variation when the effective TMAC is $\alpha \leq 0.01$. On the other hand, when the channel height is large, however, K decreases when the channel height increases, and eventually the enhancement is reduced to 1. This is because the PMMA polymer molecule tends to be absorbed on the graphene surface (see Fig. 2(d) in Ref. [13]), which forms "bumps" on the channel impeding the gas flow, and the larger the channel height, the easier and higher the bumps are formed.

Third, in the experiment [13], the mass flow rates of deuterium and hydrogen are measured and compared. It is found that the graphene channel with a height of 13.6 nm exhibited permeability $\approx (30 \pm 10)\%$ smaller for deuterium than hydrogen. Since both isotopes have the same interaction with the graphene but have different de Broglie wavelengths, they drew the conclusion that "this fact unequivocally proves that matter-wave effects contribute to the specular reflection leading

to its suppression for heavier atoms because deuterium has a shorter de Broglie wavelength and sees an atomic landscape somewhat rougher than hydrogen". Since the present work only relies on the empirical parameters in Maxwell's diffuse-specular boundary condition, this phenomenon should be explained based on the density functional theory, molecular dynamic simulation [35, 36], or advanced kinetic models for the gas-surface interaction such as the Enskog-Vlasov collision operator [37, 38] and the Boltzmann-type gas-phonon collision operator [39]. Here we point out one possible fact that, at the same temperature, the mean thermal speed of deuterium is smaller than hydrogen, and in the Epstein kinetic boundary condition [24, 40] or molecular dynamic simulations [41, 42], it can be found that larger speed molecules are less likely trapped by the wall molecules and hence a smaller effective TMAC. In other words, even without involving the quantum effect, the smaller mass flow rate of deuterium than hydrogen can be explained in terms of the relative large TMAC. This will be subject to our future work.

VI. CONCLUSIONS

In summary, we have investigated the behavior of a two-dimensional pressure-driven gas flow through a finite-length channel with rough elements in the form of rectangular bumps. The apparent gas permeability in the rough channel is obtained by solving the gas kinetic equation and Maxwell's diffuse-specular gas-surface boundary condition. Our results have shown that the properties of gas flow in rough channel are the combined result of multiple factors such as the tangential momentum accommodation coefficient (α), the size of bumps, and the channel length. The main findings could be summarized as follows:

1. In the rough channel with small value of TMAC, the pressure-driven flow could exhibit inverted streamwise velocity profile, that is, the flow velocity near the solid surface could be larger than that in the middle of the channel, see Fig. 4.

2. In the rough channel, even if the size of bumps is very small, the small disturbance caused by it can penetrate into the main flow area and affect the flow characteristic of the whole channel. Specifically, in the free-molecular regime, when the TMAC is very small, the apparent gas permeability will be dramatically reduced by the presence of bumps, to a value that is almost comparable to that of TMAC ≈ 0.5, see Fig. 7.

3. In the free-molecular regime, the end effect is rather significant when the effective TMAC of the channel is very small, such that the mass flow rate will be much reduced when the channel is not long enough, see Fig. 9. Based on the numerical simulations, we have tabulated the end correction length at typical values of TMAC and channel length in Table I, which will be useful for engineering corrections.

Based on the numerical simulations, we have properly explained the exotic mass flow rate in hBN and graphene channels, as observed in the experiment [13] and molecular dynamic simulation [19].

DATA AVAILABILITY STATEMENT

The data that support the findings of this study are available from the corresponding author upon reasonable request.

ACKNOWLEDGEMENTS

CONFLICT OF INTEREST

The authors have no conflicts to disclose.

[1] Farzam Javadpour, Douglas Fisher, and Michelle Unsworth, "Nanoscale gas flow in shale gas sediments," Journal of Canadian Petroleum Technology **46** (2007).

[2] D Sholl and R. Lively, "Seven chemiical separation to change the world," Nature **532**, 435–437 (2016).

[3] Liehui Zhang, Baochao Shan, Yulong Zhao, and Zhaoli Guo, "Review of micro seepage mechanisms in shale gas reservoirs," International Journal of Heat and Mass Transfer **139**, 144–179 (2019).

[4] Robert G Loucks, Robert M Reed, Stephen C Ruppel, and Daniel M Jarvie, "Morphology, genesis, and distribution of nanometer-scale pores in siliceous mudstones of the mississippian barnett shale," Journal of Sedimentary Research **79**, 848–861 (2009).

[5] Gaoyuan Yan, Chongtao Wei, Yu Song, Jinhui Luo, and Junjian Zhang, "Quantitative description of shale pore structure using image analysis and determination of controls on shape, size and orientation complexity," Arabian Journal of Geosciences **11**, 1–11 (2018).

[6] Mark E Curtis, Carl H Sondergeld, Raymond J Ambrose, and Chandra S Rai, "Microstructural investigation of gas shales in two and three dimensions using nanometer-scale resolution imagingmicrostructure of gas shales," AAPG Bulletin **96**, 665–677 (2012).

[7] Farzam Javadpour, "Nanopores and apparent permeability of gas flow in mudrocks (shales and siltstone)," Journal of Canadian Petroleum Technology **48**, 16–21 (2009).

[8] Hamed Darabi, Amin Ettehad, Farzam Javadpour, and Kamy Sepehrnoori, "Gas flow in ultra-tight shale strata," Journal of Fluid Mechanics **710**, 641–658 (2012).

[9] Ali Beskok and George Em Karniadakis, "Report: a model for flows in channels, pipes, and ducts at micro and nano scales," Microscale thermophysical engineering **3**, 43–77 (1999).

[10] Faruk Civan, "Effective correlation of apparent gas permeability in tight porous media," Transport in porous media **82**, 375–384 (2010).

[11] LJ Klinkenberg, "The permeability of porous media to liquids and gases," Am. Petrol. Inst., Drilling and Production Practice **2**, 200–213 (1941).

[12] J. K. Holt, H. G. Park, Y. Wang, M. Stadermann, A. B. Artyukhin, C. P. Grigoropoulos, A. Noy, and O. Bakajin, "Fast mass transport through sub-2-nanometer carbon nanotubes," Science **312**, 1034–1037 (2006).

[13] Ashok Keerthi, Andre K Geim, A Janardanan, Aidan P Rooney, Ali Esfandiar, S Hu, Sidra Abbas Dar, Irina V Grigorieva, Sarah J Haigh, FC Wang, et al., "Ballistic molecular transport through two-dimensional channels," Nature **558**, 420–424 (2018).

[14] L. Wang, M. S. H. Boutilier, P. R. Kidambi, D. Jang, N. G. Hadjiconstantinou, and R. Karnik, "Fundamental transport mechanisms, fabrication and potential applications of nanoporous atomically thin membranes," Nature Nanotechnology **12**, 509–522 (2017).

[15] W Steckelmacher, "A review of the molecular flow conductance for systems of tubes and components and the measurement of pumping speed," Vacuum **16**, 561–584 (1966).

[16] Lei Wu, Minh Tuan Ho, Lefki Germanou, Xiao-Jun Gu, Chang Liu, Kun Xu, and Yonghao Zhang, "On the apparent permeability of porous media in rarefied gas flows," Journal of Fluid Mechanics **822**, 398–417 (2017).

[17] M. Majumder, N. Chopra, and B. J. Hinds, "Mass transport through carbon nanotube membranes in three different regimes: Ionic diffusion and gas and liquid flow," ACS Nano **5**, 3867–3877 (2011).

[18] P. L. Bhatnagar, E. P. Gross, and M. Krook, "A model for collision processes in gases. i. small amplitude processes in charged and neutral one-component systems," Phys. Rev. **94**, 511–525 (1954).

[19] JianHao Qian, YiHeng Li, HengAn Wu, and FengChao Wang, "Surface morphological effects on gas transport through nanochannels with atomically smooth walls," Carbon **180**, 85–91 (2021).

[20] Reza Kamali and Ali Kharazmi, "Molecular dynamics simulation of surface roughness effects on nanoscale flows," International Journal of Thermal Sciences **50**, 226–232 (2011).

[21] Bing-Yang Cao, Min Chen, and Zeng-Yuan Guo, "Effect of surface roughness on gas flow in microchannels by molecular dynamics simulation," International Journal of Engineering Science **44**, 927–937 (2006).

[22] F. Sharipov, P. Fahrenbach, and A. Zipp, "Numerical modeling of holweck pump," J. Vac. Sci. Technol. A **23**, 1331–1339 (2005).

[23] G. PHAM-VAN-DIEP, D. Erwin, and E. P. Muntz, "Nonequilibrium molecular motion in a hypersonic shock wave," Science **245**, 624–626 (1989).

[24] L. Wu and H. Struchtrup, "Assessment and development of the gas kinetic boundary condition for the Boltzmann equation," J. Fluid Mech. **823**, 511–537 (2017).

[25] James Clerk Maxwell, "On stresses in rarified gases arising from inequalities of temperature," Philosophical Transactions of the Royal Society of London **170**, 231–256 (1879).

[26] Wei Su, Scott Lindsay, Haihu Liu, Lei Wu, et al., "Comparative study of the discrete velocity and lattice boltzmann methods for rarefied gas flows through irregular channels," Physical Review E **96**, 023309 (2017).

[27] S. Takata and H. Funagane, "Poiseuille and thermal transpiration flows of a highly rarefied gas: overconcentration in the velocity distribution function," J. Fluid Mech. **669**, 242–259 (2011).

[28] L. Wu, J. M. Reese, and Y. H. Zhang, "Solving the Boltzmann equation by the fast spectral method: application to microflows," J. Fluid Mech. **746**, 53–84 (2014).

[29] W. Su, M. T. Ho, Y. H. Zhang, and L. Wu, "GSIS: an efficient and accurate numerical method to obtain the apparent gas permeability of porous media," Comput. Fluids **206**, 104576 (2020).

[30] W. Su, L. H. Zhu, P. Wang, Y. H. Zhang, and L. Wu, "Can we find steady-state solutions to multiscale rarefied gas flows within dozens of iterations?" J. Comput. Phys. **407**, 109245 (2020).

[31] S. Pantazis, D. Valougeorgis, and F. Sharipov, "End corrections for rarefied gas flows through capillaries of finite length, (2013)." Vacuum **97**, 26 (2013).

[32] S. Pantazis, D. Valougeorgis, and F. Sharipov, "End corrections for rarefied gas flows through circular tubes of finite length," Vacuum **101**, 306–312 (2014).

[33] F. Sharipov and V. Seleznev, "Data on internal rarefied gas flows," J. Phys. Chem. Ref. Data **27**, 657–706 (1998).

[34] K. K. Kammara, R. Kumar, A. K. Singh, and A. K. Chinnappan, "Systematic direct simulation Monte Carlo approach to characterize the effects of surface roughness on accommodation coefficients," Phys. Rev. Fluids **4**, 123401 (2019).

[35] M. Barisik and A. Beskok, "Scale effects in gas nano flows," Phys. Fluids **26**, 052003 (2014).

[36] M. Barisik and A. Beskok, ""Law of the nano-wall" in nano-channel gas flows," Microfluid Nanofluid **20**, 46 (2016).

[37] A. Frezzotti and L. Gibelli, "A kinetic model for fluid wall interaction," Proc. IMechE, Part C: J. Mech. Eng. Science **222**, 787–795 (2008).

[38] P. Barbante, A. Frezzotti, and L. Gibelli, "A kinetic theory description of liquid menisci at the microscale," Kinet. Relat. Models **8**, 235–254 (2015).

[39] S. Brull, P. Charrier, and L. Mieussens, "Nanoscale roughness effect on Maxwell-like boundary conditions for the Boltzmann equation," Phys. Fluids **28**, 082004 (2016).

[40] M. Epstein, "A model of the wall boundary condition in kinetic theory," AIAA Journal **5**, 1797–1800 (1967).

[41] William W. Lim, Gregg J. Suaning, and David R. McKenzie, "A simulation of gas flow: The dependence of the tangential momentum accommodation coefficient on molecular mass," Phys. Fluids **28**, 097101 (2016).

[42] Hiroki Yamaguchi, Yu Matsuda, and Tomohide Niimi, "Molecular-dynamics study on characteristics of energy and tangential momentum accommodation coefficients," Phys. Rev. E **96**, 013116 (2017).